Sample Processing and Benchmarking for Multibeam Optical Scanning Transmission Electron Microscopy

Duinkerken, B. H.Peter; Kievits, Arent J.; Wolters, Anouk H.G.; van Beijeren Bergen en Henegouwen, Daan; Kuipers, Jeroen; Hoogenboom, Jacob P.; Giepmans, Ben N.G.

Important note
To cite this publication, please use the final published version (if applicable).
Please check the document version above.

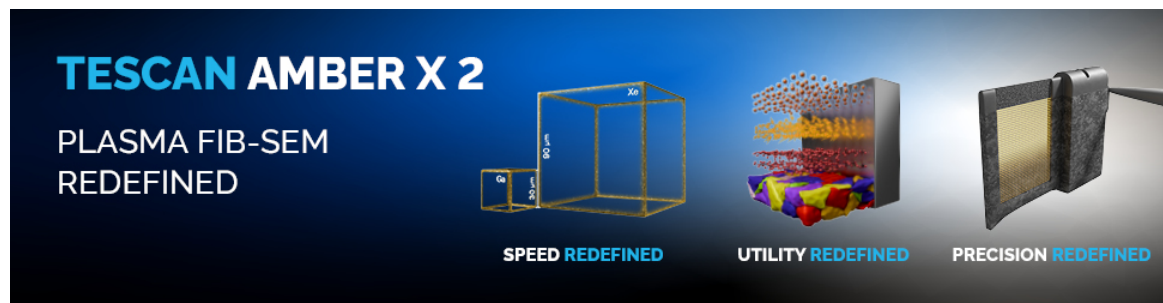# Sample Processing and Benchmarking for Multibeam Optical Scanning Transmission Electron Microscopy

B H Peter Duinkerken, Arent J Kievits, Anouk H G Wolters, Daan van Beijeren Bergen en Henegouwen, Jeroen Kuipers, Jacob P Hoogenboom, Ben N G Giepmans

Microscopy AND
Microanalysis

Sample Processing and Benchmarking for Multibeam Optical Scanning Transmission Electron Microscopy

B.H. Peter Duinkerken[1],* [ID], **Arent J. Kievits[2]** [ID], **Anouk H.G. Wolters[1]** [ID], **Daan van Beijeren Bergen en Henegouwen[1]**, **Jeroen Kuipers[1]** [ID], **Jacob P. Hoogenboom[2]** [ID], and **Ben N.G. Giepmans[1]** [ID]

[1]Department of Biomedical Sciences, University of Groningen, University Medical Centre Groningen, Antonius Deusinglaan 1, Groningen, AV 9713, The Netherlands
[2]Department of Imaging Physics, Delft University of Technology, Lorentzweg 1, Delft, CJ 2628, The Netherlands
*Corresponding author: B.H. Peter Duinkerken, E-mail: b.h.p.duinkerken@umcg.nl

Abstract

Electron microscopy (EM) is an indispensable technique to visualize biological ultrastructure in health and disease. High-throughput EM further enables larger scales and volumes to be recorded within feasible timeframes. Multibeam optical scanning transmission EM (OSTEM) utilizes multiple beamlets and optical separation of the transmitted electrons to increase imaging throughput with transmission-based imaging. However, the compatibility of multibeam OSTEM with routine sample preparation protocols and the effect of machine settings on image quality remain largely unknown. Here, we show multibeam OSTEM to be an order of magnitude faster than (scanning) transmission EM while yielding comparable high-quality images of tissue processed with standard high-contrast staining protocols. Multibeam OSTEM benefits from embedding approaches that introduce high contrast but is flexible in the type of stain used. Optimal results are obtained using an acceleration voltage of 5 kV, where section thickness and pixel dwell time require a balance between throughput and image quality. Our results show high-throughput EM with imaging quality comparable with commonly used transmission-based modalities, enabling biological ultrastructure analysis across larger scales and volumes.

Key words: electron microscopy, FAST-EM, multibeam STEM, optical STEM

Introduction

Life is regulated at the scale of biomolecules, where electron microscopy (EM) enables the ultrastructural components to be visualized and analyzed. In multicellular organisms, structure and function is organized in cells and tissues, but high-resolution imaging is traditionally limited to a small field-of-view (FOV) allowing only a fragment of a slice of a cell to be recorded at the nanoscale. Advances in technology have expanded the FOV through tiled acquisitions and provide volumetric insights via serialized acquisitions using *in situ* sectioning or array tomography approaches (Faas et al., 2012; Kuipers et al., 2016; Kievits et al., 2022; Collinson et al., 2023). Due to the time-consuming nature of such techniques, acquiring both biologically relevant FOVs and volumes is typically not feasible. Various approaches have been developed for both transmission EM (TEM) and scanning EM (SEM) to increase the acquisition throughput, by reducing overhead time, i.e., time not spent on recording, or decreasing acquisition time.

TEM camera array increases throughput by projecting the transmitted electrons indirectly on an array of cameras, expanding the FOV and thereby limiting the time spent on stage movement and settling times (Bock et al., 2011). Throughput in TEM-based approaches has since further increased by the use of faster cameras and stages (Zheng et al., 2018), faster sample handling through GridTape (Phelps et al., 2021), parallelized acquisition on multiple TEMs (Yin et al., 2020), and beam-deflection TEM that further reduces stage movements

(Zheng et al., 2024). While these advances in instrumentation have realized a throughput of up to 300 megapixels per second (Mpx/s), user-made modifications to existing microscopes are required, which may limit their accessibility and thus a broader implementation. Alternatively, acquisition times have decreased through parallelized scanning and detection in SEMs where the primary beam is split into multiple beamlets: the MultiSEM and fast automated scanning transmission EM (FAST-EM), commercialized by, respectively, Zeiss and Delmic.

The MultiSEM utilizes either 61 or 91 electron beamlets and relies on an arrayed secondary electron (SE) detector to separate the signals originating from the individual beams (Eberle et al., 2015). Next to biological applications in large-scale topological SE imaging (Pereira et al., 2016), internal ultrastructure visualization has seen implementations in renal (Dittmayer et al., 2018; Miyaki et al., 2024) and neuronal tissues (Shibata et al., 2019; Loomba et al., 2022; Günther et al., 2024). The resulting images are indeed of sufficient quality for the mapping of relatively large structures such as the renal glomerulus or axonal tracing. The capability for high-throughput mapping has recently been further underscored by the recording of a peta-voxel fragment of human brain tissue with an average throughput of 190 Mpx/s (Shapson-Coe et al., 2024). However, the restriction to SE imaging yields images with visibly less contrast compared with other detection approaches, potentially limiting its use for analysis of finer ultrastructural details (Kubota et al., 2018).

The FAST-EM creates 64 beamlets and leverages a novel optical scanning TEM (OSTEM) detection approach that

separates the individual signals arising from multibeam imaging (Zuidema & Kruit, 2020). Here, the transmitted electrons interact with a scintillating substrate in which photons are generated, which are subsequently detected through an optical system. Image formation in the FAST-EM is therefore transmission based, as opposed to SE imaging in the MultiSEM, yielding images comparable with (S)TEM with an increased throughput compared with single-beam imaging (de Boer & Giepmans, 2021; Kievits et al., 2024b).

Routine and optimal implementations of FAST-EM in biomedical research, however, require a more elaborate analysis of the effect that sample preparation and imaging parameters have on image quality and contrast. Therefore, we subjected FAST-EM to various staining routines and imaging parameters and compare the results with traditional TEM-based and scanning transmission EM (STEM)–based large-scale EM.

Materials and Methods

Tissue Preparation

Rat pancreas tissue was fixed and stored in 2% paraformaldehyde (104005, Merck) and 0.5% glutaraldehyde (01909, Polysciences) dissolved in 0.1 M sodium cacodylate (20840, Sigma-Aldrich) buffer (pH 7.4) at 4°C. Prior to embedding, tissue was placed in 4% low melt agarose (H26417, Alfa Aesar) in cacodylate buffer and sectioned at a thickness of 50 μm using a vibratome (VT1000S, Leica). Tissue was postfixed using 1% osmium tetroxide (osmium; 19114, Electron Microscopy Sciences) with 1.5% potassium ferrocyanide (P9387, Merck) in cacodylate buffer for 2 h at 4°C. The reduced osmium, thiocarbohydrazide, and osmium (rOTO) processed samples were postfixed in the same solution with an additional 4 mM calcium chloride (C1016, Sigma-Aldrich) and incubated for 1 h at 4°C, followed by: (i) four washes with MilliQ water (MQ); (ii) exposure to 0.22 μm-filtered 1% thiocarbohydrazide (T2137, Sigma-Aldrich) solution in MQ for 20 min at room temperature (RT); (iii) three more MQ washes; and (iv) a half hour incubation with 1% osmium in MQ at RT. For the sequentially reduced samples, the initial osmium incubation step was replaced with sequential exposure to 1% osmium in cacodylate buffer followed by 1.5% potassium ferrocyanide in cacodylate buffer after removal of osmium, for 90 min each at RT. After postfixation, all samples were washed thrice in MQ and dehydrated using a graded ethanol series and two acetone incubation steps. EPON resin infiltration was facilitated by overnight incubation of tissue with a 1:1 dilution of EPON in acetone. After three 1 h incubations with pure EPON the following day, samples were placed between Aclar sheets and allowed to polymerize at 58°C. Samples were sectioned (ARTOS 3D, Leica) with a jumbo diamond knife (AT4, Diatome) at a thickness of 100 nm, unless noted otherwise. The scintillator was fully submerged in the jumbo diamond knife prior to sectioning, and sections were deposited by lowering of the water level.

Staining

Pre-embedding staining was achieved by immersion of the tissue into aqueous solutions of 2% uranyl acetate (8473, Merck), 4% neodymium acetate (325805, Sigma-Aldrich), 4% samarium acetate (325678, Sigma-Aldrich), 4% gadolinium acetate (325678, Sigma-Aldrich), 4% hafnium chloride (258202, Sigma-Aldrich), 1% potassium permanganate (60459, Fluka BioChemika), or Uranyless (22409, Electron

Microscopy Sciences), based on previous studies (Sutton, 1968; Hatae et al., 1984; Ikeda et al., 2011; Nakakoshi et al., 2011; Hosogi et al., 2015; Kaku et al., 2015; Odriozola et al., 2017; Kuipers & Giepmans, 2020; Moscardini et al., 2020; Ishii, 2022; Ishii & Odahara, 2023; Sawaguchi et al., 2024). Staining was conducted following the osmium washes by exposing the tissue to the staining solution overnight at 4°C except for potassium permanganate, which was done for 1 h. For the warm incubation experiments, the tissue was incubated at 58°C for 2 h following the initial 4°C overnight exposure. Tissue samples were additionally stained with lead aspartate, 0.02 M lead nitrate (3671499, Merck) in 0.03 M aspartic acid (A7219, Sigma-Aldrich), for 30 min at 58°C (Walton, 1979). Following staining, samples were dehydrated as described (Kievits et al., 2024a). For the postembedding staining test, sections deposited on cerium-doped yttrium-aluminum garnet (YAG:Ce) were exposed to 4% neodymium acetate for 30 min at RT, followed by three washes with MQ and allowed to air dry.

Multibeam OSTEM

Ultrathin sections were deposited on YAG:Ce substrates (Delmic) as indicated (Supplementary Fig. S1a). Except for Figure 2a, all FAST-EM data in figure panels were derived from sections deposited on the same substrate. Images were acquired on an early adopter system of the Delmic FAST-EM, based on a Thermo Fisher Scientific Apreo SEM modified for multibeam imaging and OSTEM detection (Kievits et al., 2024b). Delmic ODEMIS software v3.4 was used to acquire images with a dwell time of 10 μs, at 5 kV, and a multipixel photon counter (MPPC) array overvoltage of 2.3 V, unless otherwise noted. The dark offset and digital gain are recalibrated following each change in MPPC overvoltage after which the same region of interest was acquired. All datasets are composed of a large-scale acquisition of 5 × 5 fields for a total of 1,600 beamlet tiles, except for the MPPC overvoltage experiments where a total of 4 × 4 fields (1,024 beamlet tiles) were acquired.

Brightfield TEM

Ultrathin sections were deposited on single-hole copper grids (G2010-CU, Electron Microscopy Sciences) with a formvar support film. TEM acquisitions were done on a Thermo Fisher Scientific Talos F200i S/TEM at 80 kV and a measured screen current of ~3–4 nA. Thermo Fischer Scientific Velox v3.12 and MAPS v3.28 software were used to capture images with a Ceta 16 M speed camera in which five consecutive 200-ms exposures were combined. Prior to imaging, the region of interest was preirradiated for 1 h with a screen current of 30–40 nA to limit the effect of beam damage on the sample, manifesting as local brightening in the image.

Darkfield STEM

The same section that was imaged with brightfield TEM (BF-TEM) was imaged with darkfield STEM (DF-STEM) using a Zeiss Supra 55 with a DF-STEM detector. Images were acquired at 25 kV with a 30-μm aperture, a measured probe current of 170 pA, and a pixel size and dwell time of 4 nm and 3 μs, respectively. Zeiss ATLAS software v5.2 was used for the large-scale acquisition.
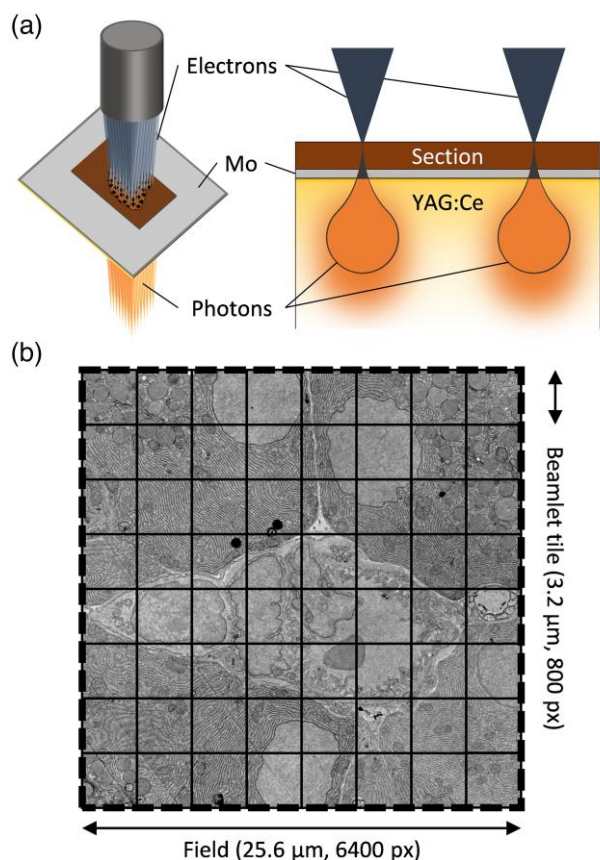
Fig. 1. Image formation in multibeam OSTEM. (**a**) An 8 × 8 array of 64 electron beamlets scan on ultrathin section deposited on a cerium-doped yttrium-aluminum garnet (YAG:ce) scintillator coated with a conductive 30 nm molybdenum layer. Transmitted electrons generate photons in the scintillating substrate that are detected by optics and thereby allow separation of the individual signals as further detailed in the study by Kievits et al., (2024b). (**b**) Each beamlet generates an image, a beamlet tile, with a set pixel size of 4 nm. While beamlet tiles do overlap in the process, automatic stitching results in an output of a single field image of 6,400 × 6,400 pixels.

Software

Image processing and metric calculations were done in Python v3.12.3 using Jupyter v4.2.1 (Granger & Perez, 2021). Images were imported and exported using Tifffile v2024.9.20 (Gohlke, 2024) and intermediately stored and handled with NumPy v1.26.4 (Harris et al., 2020). Metrics were calculated using NumPy, Dask v2024.8.2 (Rocklin, 2015), OpenCV v4.10 (Bradski, 2000), and scikit-image v0.22 (van der Walt et al., 2014).

Image Processing

The median field image was calculated for each individual mosaic acquisition and subtracted from the raw field images to correct for residual uneven brightness and beam damage artifacts. The BF-TEM was similarly processed to correct for uneven radial illumination. The corrected images were subsequently normalized from 0 to 255 where the 0.5th and 99.5th percentiles of pixel values were allowed to saturate.

Metrics

Metrics were calculated for each beamlet tile individually, and the distribution within a single dataset, originating from an experimental condition, was plotted. All metrics were calculated based on the median-corrected images, as described above, without further normalization. Contrast is defined as the spread of pixel intensities within a beamlet tile, where the interquartile range (IQR) is used as a measure of spread. Noise was estimated by calculating the root of the mean squared difference between the original beamlet tile and its Gaussian-blurred ($\sigma = 1$) variant (Supplementary Fig. S3a). The contrast to noise ratio (CNR) reflects the quotient of contrast and noise. For plotting purposes, both contrast and noise were divided by 1,000. Beamlet tiles with abnormal contrast, dark pixels, or light pixels were excluded. Here, the 0.5th and 99.5th percentiles of pixel values were considered dark and light pixels, respectively. Beamlet tiles with values exceeding Tukey's fences within the respective category were excluded. Furthermore, edge detection was employed to select the images presented in Figures 2 and 3 and Supplementary Fig. S2; the beamlet tile with the highest standard deviation after subjecting it to a Gaussian blur ($\sigma = 2$) and a subsequent Laplacian kernel ($k = 3$), excluding outliers based on Tukey's fences, was selected. Edge detection was employed to automatically select images with sharp edges, which (i) allows the subjectivity associated with handpicking images to largely be avoided and (ii) enables images with sharp edges, i.e., in-focus membranes, to be selected. Throughput and acquisition time are based on the difference between the timestamp of the last file and the first file, normalized against the number of pixels present in the files that were acquired within this timeframe. The files contain the field images for FAST-EM acquisitions and tiles for DF-STEM and BF-TEM.

Results

Multibeam OSTEM Imaging With the FAST-EM

FAST-EM utilizes an 8 × 8 array of beamlets to simultaneously scan a section, an ultrathin slice of fixed and heavy atom stained bio-sample embedded in EPON, placed on top of a molybdenum-coated (30 nm) scintillator. Routing of the photons generated by transmitted electrons to a MPPC array enables parallelized acquisition of 64 images (beamlet tiles). Automatic stitching of the beamlet tiles yields a single field image with an FOV of 25.6 μm (Fig. 1b), which is further expanded by stage movements to form a mosaic (Kievits et al., 2024b). Sample preparation, including choice of heavy atom staining and section thickness, as well as acquisition settings such as dwell time and acceleration voltage, will influence image formation specific to the novel detection approach.

Heavy Metal Staining Is Beneficial for FAST-EM Contrast

Biological tissue is primarily composed of light elements that are not optimal for contrast generation in EM. Heavy metal osmium tetroxide (osmium) incorporation not only fixes the membrane lipids but also introduces additional localized electron density. To evaluate membrane contrast, exocrine pancreas tissue is ideal because, besides the more general ultrastructural features (e.g., mitochondria, granules, etc.), there is an abundance of rough endoplasmic reticulum (ER) where multiple membranes are closely associated but sufficiently spaced (generally >10 nm) to be resolved (West et al., 2011). Tissue was imaged with FAST-EM to address the effect of osmium-based fixation on image quality (Fig. 2a). ER is discernible but contrast is limited when
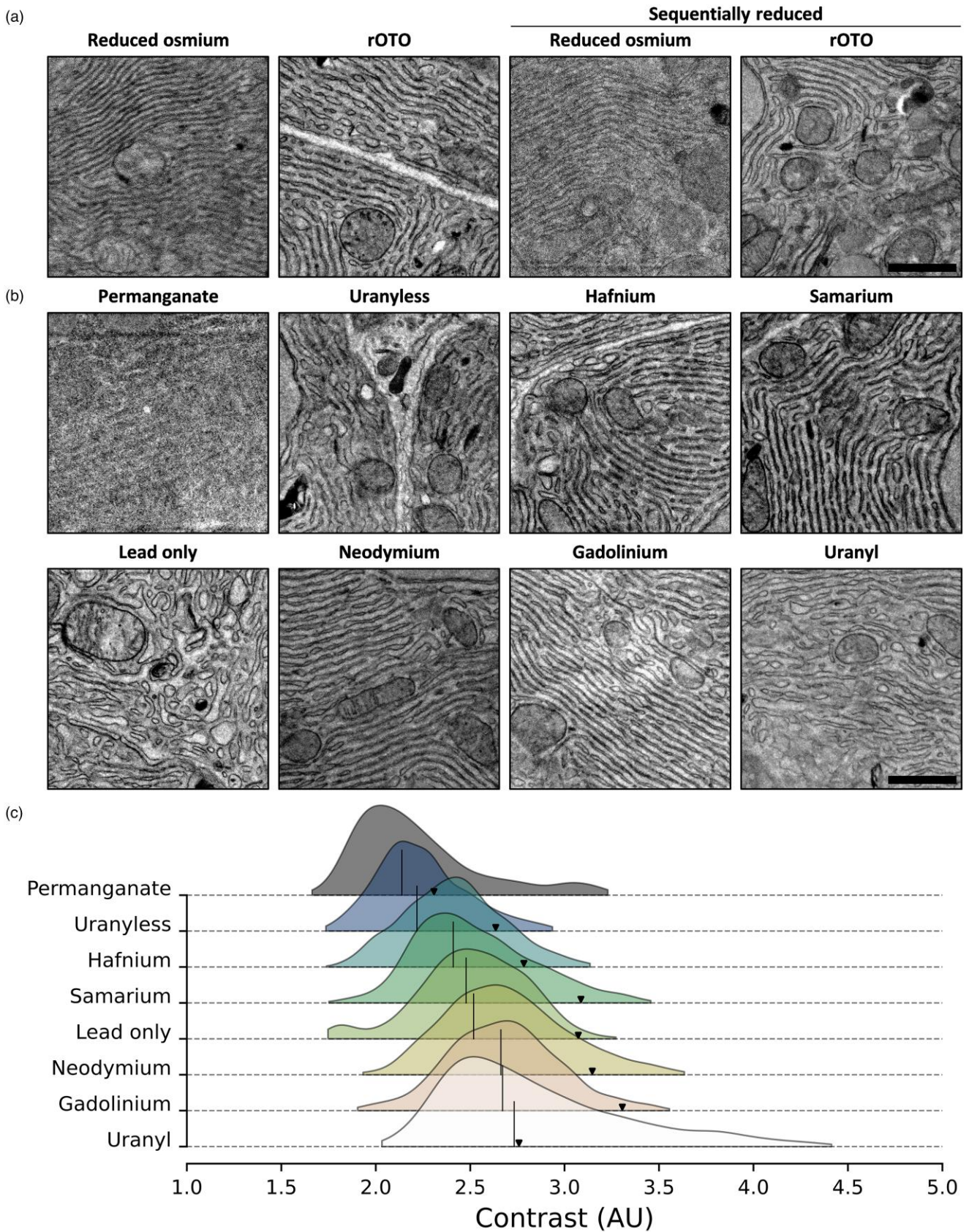
Fig. 2. FAST-EM benefits from heavy contrast and is compatible with various pre-embedding stains. (**a**) Beamlet tiles of rat pancreas tissue stained with either reduced osmium or rOTO, with or without the sequential addition of potassium ferrocyanide. All samples were subsequently stained with both neodymium and lead prior to EPON embedding. (**b**) Beamlet tiles of tissue were embedded with rOTO, and pre-embedding was treated with the indicated stains and lead. (**c**) Distribution of beamlet tile contrast values; note that contrast here represents the spread of pixel values for each beamlet tile. Black lines indicate the median contrast across all beamlet tiles, and triangle indicates the corresponding contrast value of the beamlet tile as shown in (**b**). Beamlet tiles with the highest number of edges are shown (see *Materials and Methods*). All images were normalized with saturation of the 1st and 99th percentiles of pixel intensities of the whole individual datasets. Bar: 1 μm. Large-scale datasets at full resolution can be retrieved at nanotomy.org.

tissue is treated with potassium ferrocyanide reduced osmium like for traditional TEM. Amplification of osmium deposition through the consecutive exposure of tissue to rOTO enhances the membrane contrast, allowing ultrastructure to be readily assessed (Seligman et al., 1966; Willingham & Rutherford, 1984; Briggman et al., 2011; Holcomb et al., 2013). Deposition of rOTO processed samples on molybdenum-coated YAG:Ce substrates may yield crystalline electron–dense artifacts that can be prevented by depositing the sections in the water bath of the diamond knife instead of using the "perfect loop" approach (Supplementary Fig. S1a). The *in situ* reduction of osmium through the sequential, instead of premixed, addition of osmium and potassium ferrocyanide has previously been shown to enhance contrast and facilitate staining of volumetric samples (Hua et al., 2015). While slightly reducing apparent image contrasts, sequentially reducing osmium yields sufficient contrast for ultrastructure to be inspected.

Staining with additional heavy metals expands the discernibility of the ultrastructure. In the aforementioned experiments (Fig. 2a), the tissue was stained *en bloc*, that is through immersion prior to embedding and thus further referred to as pre-embedding staining, with neodymium and lead to enhance contrast (Kuipers & Giepmans, 2020). Using neodymium acetate as a postembedding stain, where sections deposited on YAG:Ce are exposed to the staining solution, yields nonbiological electron dense features that obscure the underlying ultrastructure (Supplementary Fig. S1b). Various other contrasting agents have been explored, primarily to overcome the radioactivity and limited availability of uranyl acetate. To test the compatibility of such stains with FAST-EM, imaging was conducted on rat pancreas pre-embedding stained with lead alone or combined with a subset of previously explored stains: uranyl acetate, potassium permanganate, hafnium chloride, samarium acetate, neodymium acetate or gadolinium acetate, and a commercially available uranyl acetate alternative called Uranyless. All stains provide sufficient contrast for FAST-EM imaging, but potassium permanganate appears detrimental for the ultrastructure (Fig. 2b). Each dataset (25 fields × 64 tiles, thus 1,600 individually acquired beamlet tiles) provide sufficient data for the quantification of contrast, for which the IQR of pixel values of each beamlet tile is taken. Tissue stained with lead together with neodymium, gadolinium, or uranyl shows higher contrast values compared with tissue stained with lead alone (Fig. 2c). Potassium permanganate, Uranyless, hafnium, and samarium diminish the contrast compared with lead alone. Staining at an elevated temperature following an initial cold incubation has previously been shown to further enhance contrast for uranyl (Hua et al., 2015). However, a subsequent warm incubation does not affect neodymium contrasting and only slightly benefits uranyl contrasting, based on apparent image quality (Supplementary Fig. S2a) and measured contrast (Supplementary Fig. S2b). Taken together, FAST-EM imaging is compatible with multiple staining protocols, and image quality is positively affected by the introduction of heavy contrast.

Effect of Section Thickness and Acceleration Voltage on FAST-EM Imaging

Contrast formation in OSTEM relies on the spatial difference in the number of electrons that are transmitted and thus results in photon generation. Besides the elemental composition, the sample thickness and acceleration voltage affect the transmission coefficient (Brodusch & Gauvin, 2024). To address their effect on FAST-EM imaging, both parameters were varied on the rOTO-embedded tissue stained with neodymium and lead. The optimal MPPC overvoltage was selected for each tested section thickness (60, 80, 100, and 120 nm) and acceleration voltage (3, 5, and 7 kV) by measuring the Gaussian-suppressed noise in the image (Supplementary Fig. S3a). While in general an increased MPPC overvoltage reduced the noise, the highest tested MPPC overvoltage typically yielded oversaturated beamlet tiles as observed and further evidenced by the tailed distribution of the noise values. Therefore, in general, the second highest MPPC overvoltage was chosen (Supplementary Figs. S3b–S3d). At 3 kV, the boundaries between membranes and the surrounding cytosol become less apparent in all the tested section thicknesses (Fig. 3a). Contrary to 3 kV, imaging at 7 kV yields clear boundaries but with diminished contrast. Images with the best appearance are obtained at 5 kV, where thinner sections provide crisper images. Indeed, the CNR is highest for 5 kV imaging and increases with section thicknesses (Fig. 3b). While the same trend is observed at 7 kV, CNR remains relatively unaffected by section thickness at 3 kV. Furthermore, the increase in CNR with section thickness appears to plateau when using sections thicker than 100 nm. Thus, 100-nm thick sections in combination with an acceleration voltage of 5 kV and MPPC overvoltage of 2.5 V yield the best results out of the tested conditions.

Balancing Throughput With Image Quality

Image quality is additionally affected by the pixel size, beamlet current, and dwell time and is therefore a tradeoff between the ultrastructure that is desired to be visualized and the imaging throughput. Since pixel size and beamlet current are fixed at 4 nm and 0.4 nA in FAST-EM, only the dwell time is customizable. Image quality with exponentially increasing dwell times on a 100-nm section and a MPPC overvoltage of 2.5 V was analyzed. At the lowest available dwell time of 1 μs, the individual membranes of the ER are resolvable (Fig. 4a). The resulting throughput of 16.1Mpx/s corresponds to 2.5 s for a single field, enabling a 1 mm^2 region to be imaged in <1.5 h (Fig. 4b). Finer details such as the membranes of mitochondrial cristae start to become visible at dwell times of 4 μs and are readily resolved at 8 μs. Further increasing the dwell time comes at the cost of lower throughput, and while this does yield visibly smoother images and increase CNRs, no further ultrastructural details are revealed (Fig. 4c). Therefore, FAST-EM imaging at 8 μs provides a sufficient level of ultrastructural detail for pancreatic exocrine tissue while reducing throughput by a factor of ∼3 (5.3 Mpx/s) compared with a 1-μs dwell time.

Image Quality of the FAST-EM Compares to (S)TEM

FAST-EM imaging with the optimized settings potentially allows much faster large-scale (S)TEM compared to more routine methods. To also compare the image quality with the most commonly used transmission-based large-scale imaging modalities the same tissue was analyzed (Table 1). Our current state of the art is DF-STEM (using a transmission detector in a SEM) and therefore compared with FAST-EM imaging. Large-scale BF-TEM was additionally conducted since it is commonly applied in biomedical research, although not routinely implemented for large-scale imaging in our lab. An area of ∼250 × 250 μm pancreas, containing a cross-section of an islet of Langerhans and surrounding exocrine tissue, was recorded.
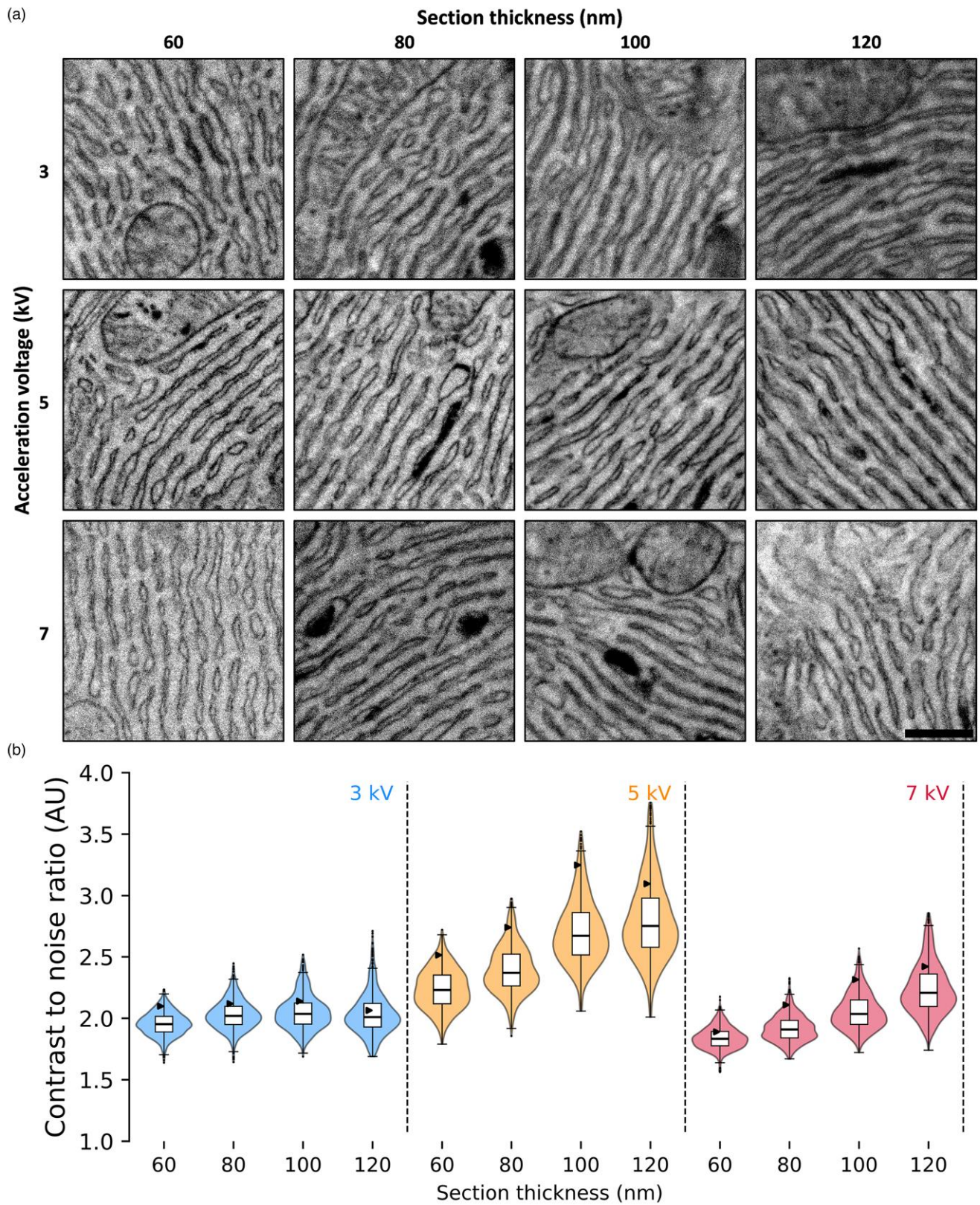
Fig. 3. Section thickness and acceleration voltage affect FAST-EM image quality. (**a**) Quarter of beamlet tile of rOTO-embedded pancreas, pre-embedding stained with neodymium and lead, at 60, 80, 100, or 120 nm thickness and imaged with 3, 5, or 7 kV. Beamlet tiles with the highest number of edges are shown (see *Materials and Methods*). All images were normalized with saturation of the 1st and 99th percentiles of pixel intensities of the whole individual datasets. Complete datasets are available at full resolution on nanotomy.org. (**b**) Distribution of beamlet tile contrast to noise ratios. Black lines indicate the median CNR, and the triangle indicates the corresponding CNR of the beamlet tile as shown in (**a**).

(a)

Dwell time (µs)
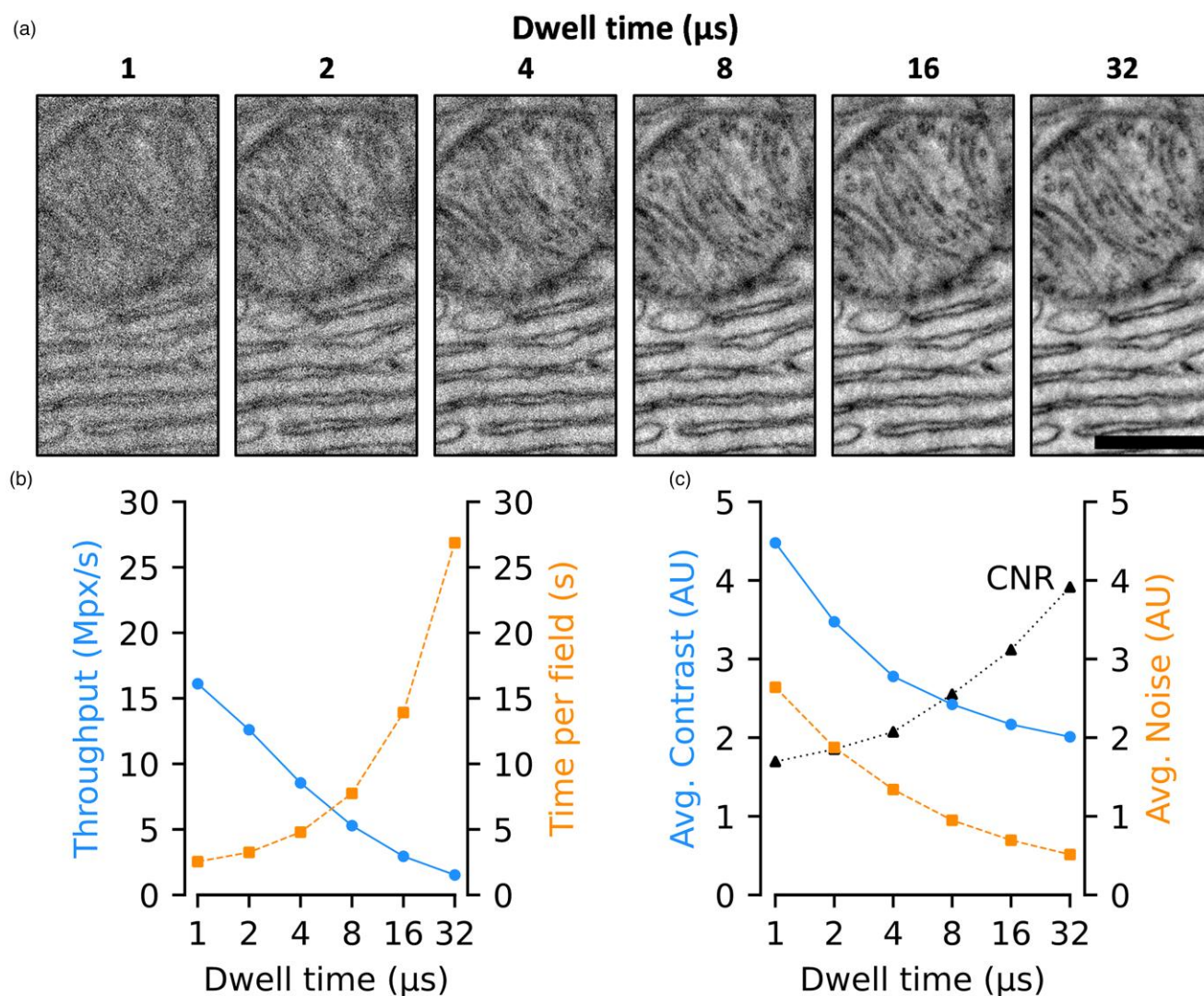
| 1 | 2 | 4 | 8 | 16 | 32 |

(b)

(c)

Fig. 4. The effect of pixel dwell time on image quality pancreas using rOTO and pre-embedding stained with neodymium and lead, sectioned at a thickness of 100 nm and imaged at a pixel size and beamlet current of, respectively, 4 nm and 0.4 nA. (**a**) Mitochondrion and rough ER reimaged with exponentially increasing dwell times. All images were normalized with saturation of the 1st and 99th percentiles of pixel intensities of the individual datasets. Bar: 0.5 μm. (**b**) Imaging throughput in Mpx/s (blue, circles with solid line) and seconds to acquire a single field (orange, squares with dashed line). Next to dwell time, acquisition includes stage movement and settling overhead, but excludes overhead such as calibrations and setup time. (**c**) Average contrast (blue, circles with solid line), noise (orange, squares with dashed line), and CNR (black, triangles with dotted line) for exponentially increasing dwell times.

Table 1. Instrumentation and Acquisition Details Used for Benchmarking Large-Scale Multibeam OSTEM (MB-OSTEM) Compared With DF-STEM, the Current Standard on nanotomy.org, and BF-TEM.

	MB-OSTEM	DF-STEM	BF-TEM
Instrument	FAST-EM	Supra 55	Talos F200i
Software	ODEMIS	Atlas	MAPS
File format	16 bit TIFF	16 bit TIFF	16 bit TIFF
Pixel size (nm)	4	4	3
Total pixels (Gpx)	4.5[a]	4.6	8.5
Stitched area (μm)	242×266	253×251	256×251
Dwell time (μs)	8	3	—
Exposure time (s)	—	—	1 (5 × 0.2)
Time (h:min)	0:14	4:43	3:53
Throughput (Mpx/s)	5.3[a]	0.27	0.60

DF-STEM is routinely implemented with a pixel size of 2.5 nm, but 4 nm was chosen here for a fairer comparison. Additionally, large-scale BF-TEM is conducted at the lowest available pixel size of 3 nm.
[a]Excluding beamlet tile overlap.

Imaging throughput was ∼5.3 (FAST-EM), 0.60 (BF-TEM), and 0.27 (DF-STEM) Mpx/s. All three imaging modalities are capable of visualizing ultrastructural components such as the ER, mitochondria, and hormone-containing granules. FAST-EM and BF-TEM yield qualitatively comparable images, whereas images generated with DF-STEM appear sharper (Fig. 5a). Note that also innervated vasculature and extracellular matrix are present (Fig. 5b). Endothelial cells in the vasculature contain caveolae, small invaginations in the plasma membrane, that are clearly visualized using DF-STEM but are increasingly difficult to distinguish with, respectively, BF-TEM and multibeam OSTEM (Fig. 5b). Fine ultrastructural details, such as the granularity of heterochromatin and the intermembrane space around axons, are mostly lost in multibeam OSTEM. Furthermore, patterns within both the internal elastic lamina and the collagen-containing extracellular matrix are appreciated in (S)TEM images but are less distinguishable in FAST-EM images. Taken together, despite the slightly decreased ability
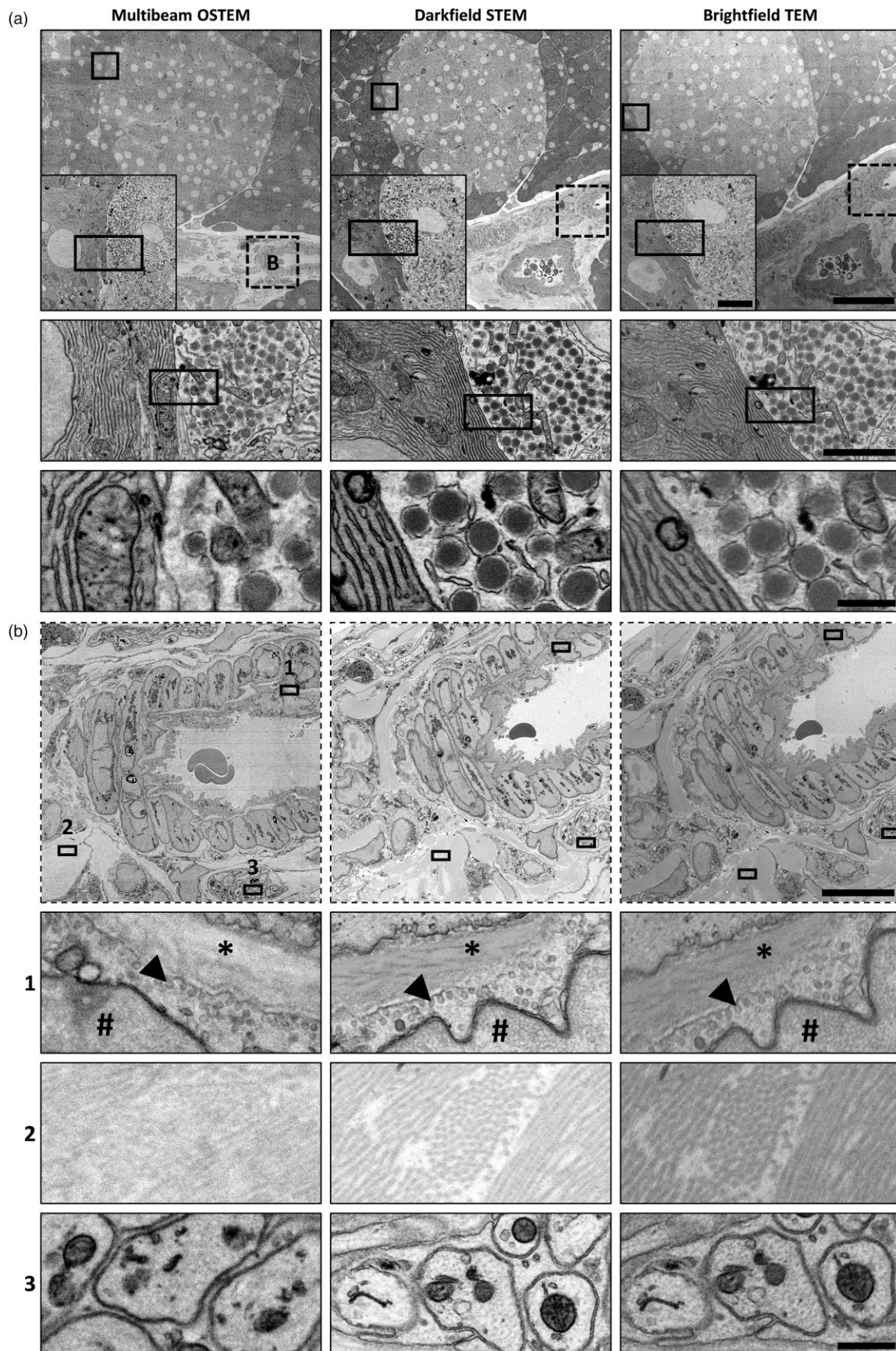
Fig. 5. Benchmarking FAST-EM, DF-STEM, and BF-TEM shows comparable output pancreas stained with rOTO neodymium and lead. (**a**) Mosaic with multiple zoom levels of exocrine and endocrine tissue acquired with multibeam OSTEM, DF-STEM, and BF-TEM. Bars: 50, 5, 2.5, and 0.5 μm. (**b**) Innervated vasculature showing the (1) internal elastic lamina (*), caveolae (arrowhead), and heterochromatin (#); (2) collagen; and (3) axons. All images were normalized with saturation of the 1st and 99th percentiles of pixel intensities of the individual datasets. Bars: 10 and 0.5 μm.

to resolve finer ultrastructural details, throughput is increased 9–20-fold compared with the alternative more common transmission imaging approaches.

Discussion and Conclusions

Large-scale imaging in EM is being routinely implemented since a decade. Despite huge benefits (automated acquisition of multiple sections, large data that allow quantification, analysis at high resolution in the context of tissue etc.), a common bottleneck precluding routine volumetric large-scale EM is the long acquisition time. Several approaches have been introduced to overcome this limitation but are typically not routinely available due to the high technical expertise and monetary investments needed. FAST-EM is a promising alternative, but tailored sample preparation and benchmarking were not explored previously.

Introducing heavy contrast in biosamples positively affects FAST-EM image quality, as evidenced by the superior quality obtained with rOTO-embedded tissue compared with reduced osmium alone. The deposition of additional osmium likely increases the amount of backscatter electrons, facilitating contrast formation in OSTEM imaging (Niedrig, 1978). Indeed, heavy contrasting procedures such as the rOTO protocol are already widely used in volume EM approaches to both increase contrast and limit charging of the sample (Hua et al., 2015). However, care must be taken in the deposition of sections with heavily contrasted tissue to prevent the formation of electron dense crystals that obscure the ultrastructure. Contrast was slightly reduced when osmium and potassium ferrocyanide were sequentially applied, potentially due to washout of osmium mediated by potassium ferrocyanide (Ströh et al., 2022). While the sequential incubation is suggested to increase contrast by the preferential washout of cytosolic osmium, using $50\,\mu m$ thin vibratome sections likely facilitated a more extensive washout. Ultrastructural analysis was impaired when tissue was stained with reduced osmium only, suggesting suboptimal results will likely be obtained on archived embedded tissue on which no emphasis was given to the introduction of heavy contrast.

Additional staining following osmium is common in EM sample preparation. FAST-EM is compatible with a multitude of stains, which we applied prior to EPON embedding. Pre-embedding staining is favorable since (i) a tissue piece is stained once, which increases throughput and (ii) staining of the thin sections on YAG:Ce substrates is prone to the formation of artifacts, likely caused by staining solution getting trapped between the section and the substrate during staining. Of the eight tested staining conditions, only potassium permanganate appears to negatively affect the ultrastructural preservation. Despite being able to enhance lead staining in paraffin sections (Sawaguchi et al., 2024) and its historical use as a post-embedding stain (Sutton, 1968), potassium permanganate as a pre-embedding stain is thus discouraged for EM analysis in general. All other pre-embedding stains yielded satisfactory results.

Acceleration voltage determines interaction volume of the electron beam and is tightly tied to resolution, whereas section thickness determines the volume of interest and the structures that can be resolved. Five kilo volts imaging provide the best qualitative results for all tested section thicknesses, as further confirmed by the CNRs. Note that only 3, 5, and 7 kV were tested due to the requirement of manufacturer intervention to change the acceleration voltage. Importantly, previous studies have shown theoretical and experimental optima in the range of 3.5–5 kV in single-beam OSTEM for different biosamples and substrates, indicating the optima will depend on the experimental conditions used (Zuidema & Kruit, 2020; Kievits et al., 2024a). Section thickness is a tradeoff between overall image smoothness and sharpness, as the increased density of structures within the volume of the section allows a greater depth of grayscale values but obscures finer details. Loss of finer details additionally impacts the axial resolution in volume EM, whereas thinner sections increase the risk of loss of material and sections during cutting. Similarly, pixel dwell time requires the throughput to be balanced against the cellular ultrastructure that is intended to be visualized but may be further reduced in the future using higher beamlet currents. Noise is estimated based on the assumption that the Gaussian-suppressed high frequency variation in the image is mostly made up of noise. While signal is likely a contributor too, the calculated noise values do reflect the qualitative observations. The CNR reveals that noise has a large contribution to the image contrast recorded at lower dwell times, since both noise and contrast decrease with increasing dwell times. Doubling the dwell time does not half the throughput indicating the overhead component becomes a substantial part of the acquisition time for lower dwell times.

Multibeam OSTEM shows a slight decrease in ultrastructural resolvability compared with DF-STEM and BF-TEM. Importantly, contrast generation in both DF-STEM and BF-TEM is not only based on whether electrons are transmitted but also based on their degree of scattering. The contribution of transmitted electrons that are differently scattered on multibeam OSTEM image formation remains to be further explored. Avoiding scintillator saturation, as indirectly observed in the study by Kievits et al. (2024a), may further enhance image formation. Additionally, the reflectivity of the molybdenum coating potentially aids in directing photons toward the MPPC, but the effect of its increased electron density is unknown. While image quality is slightly reduced compared with DF-STEM and BF-TEM, throughput is increased by 9–20-fold. The increase in throughput is likely even higher since both BF-TEM and DF-STEM (i) required preirradiation (see *Materials and Methods*) and (ii) are less compatible with multisection acquisitions such as in array tomography. Even though the FAST-EM is still outpaced by the high-throughput TEM-based and MultiSEM imaging approaches, future updates of the system will likely narrow this gap by reducing the available dwell time to $0.4\,\mu s$, increasing the beamlet current by 2.5-fold to 1 nA and allowing more freedom in choosing the acceleration voltage. Furthermore, modeling and understanding image formation in multibeam OSTEM may further increase throughput and/or the quality of the recorded images by improving the ability to resolve finer details.

Taken together, the relatively young age of the FAST-EM (we used the first early adopter system), its commercial availability, and high image quality allows transmission-based imaging an order of magnitude faster than routine techniques such as BF-TEM and DF-STEM. Even though sample preparation has to be adapted to protocols that introduce high contrast, the improved speed enables both large-scale 2D and volume EM acquisitions of ultrastructure in a timely manner.

Availability of Data and Materials

All data are available at full resolution via http://www.nanotomy.org.

Author Contributions Statement

B.H.P.D., A.J.K., and A.H.G.W. conducted the investigation. J.K. assisted and advised on the sample preparation; D.v.B.B.e.H. assisted in the acquisition; B.H.P.D. and A.H.G.W. performed the experiments. B.H.P.D. wrote the software to analyze the data. B.H.P.D. wrote the original draft. J.P.H. and B.N.G.G. acquired the funding and supervised the work. B.N.G.G. was responsible for the project administration. All authors conceptualized the study and reviewed and edited the manuscript.

Conflict of Interest

J.P.H. is a cofounder and shareholder of Delmic BV, which commercializes the FAST-EM. The NWO-ENPPS.LIFT.019.030 grant contains contribution of Delmic BV. All other authors declare that they have no competing interest.

References

Bock DD, Lee W-CA, Kerlin AM, Andermann ML, Hood G, Wetzel AW, Yurgenson S, Soucy ER, Kim HS & Reid RC (2011). Network anatomy and in vivo physiology of visual cortical neurons. *Nature* **471**, 177–182. https://doi.org/10.1038/nature09802

Bradski G (2000). The OpenCV library. *Dr. Dobb's J Softw Tool* **120**, 122–125. https://github.com/opencv/opencv/wiki/CiteOpenCV

Briggman KL, Helmstaedter M & Denk W (2011). Wiring specificity in the direction-selectivity circuit of the retina. *Nature* **471**, 183–188. https://doi.org/10.1038/nature09818

Brodusch N & Gauvin R (2024). Low voltage scanning transmission electron microscopy as a viable tool for routine analysis of materials science specimens. *Microsc Microanal* **30**, 677–678. https://doi.org/10.1093/mam/ozae044.323

Collinson LM, Bosch C, Bullen A, Burden JJ, Carzaniga R, Cheng C, Darrow MC, Fletcher G, Johnson E, Narayan K, Peddie CJ, Winn M, Wood C, Patwardhan A, Kleywegt GJ & Verkade P (2023). Volume EM: A quiet revolution takes shape. *Nat Methods* **20**, 777–782. https://doi.org/10.1038/s41592-023-01861-8

de Boer P & Giepmans BN (2021). State-of-the-art microscopy to understand islets of Langerhans: What to expect next? *Immunol Cell Biol* **99**, 509–520. https://doi.org/10.1111/imcb.12450

Dittmayer C, Völcker E, Wacker I, Schröder RR & Bachmann S (2018). Modern field emission scanning electron microscopy provides new perspectives for imaging kidney ultrastructure. *Kidney Int* **94**, 625–631. https://doi.org/10.1016/j.kint.2018.05.017

Eberle AL, Mikula S, Schalek R, Lichtman J, Knothe Tate ML & Zeidler D (2015). High-resolution, high-throughput imaging with a multibeam scanning electron microscope. *J Microsc* **259**, 114–120. https://doi.org/10.1111/jmi.12224

Faas FGA, Avramut MC, van den M, Berg B, Mommaas AM, Koster AJ & Ravelli RBG (2012). Virtual nanoscopy: Generation of ultra-large high resolution electron microscopy maps. *J Cell Biol* **198**, 457–469. https://doi.org/10.1083/jcb.201201140

Gohlke C (2024). cgohlke/tifffile: v2024.9.20. https://doi.org/10.5281/zenodo.13820913

Granger BE & Perez F (2021). Jupyter: Thinking and storytelling with code and data. *Comput Sci Eng* **23**, 7–14. https://doi.org/10.1109/MCSE.2021.3059263

Günther A, Haverkamp S, Irsen S, Watkins PV, Dedek K, Mouritsen H & Briggman KL (2024). Species–specific circuitry of double cone photoreceptors in two avian retinas. *Commun Biol* **7**, 992. https://doi.org/10.1038/s42003-024-06697-2

Harris CR, Millman KJ, van der Walt SJ, Gommers R, Virtanen P, Cournapeau D, Wieser E, Taylor J, Berg S, Smith NJ, Kern R, Picus M, Hoyer S, van Kerkwijk MH, Brett M, Haldane A, del Río JF, Wiebe M, Peterson P, Gérard-Marchant P, Sheppard K, Reddy T, Weckesser W, Abbasi H, Gohlke C & Oliphant TE (2020). Array programming with NumPy. *Nature* **585**, 357–362. https://doi.org/10.1038/s41586-020-2649-2

Hatae T, Okuyama K & Fujita M (1984). Visualization of the cytoskeletal elements in tissue culture cells by bloc-staining with hafnium chloride after rapid freezing and freeze-substitution fixation. *J Electron Microsc (Tokyo)* **33**, 186–190. https://doi.org/10.1093/oxfordjournals.jmicro.a050456

Holcomb PS, Hoffpauir BK, Hoyson MC, Jackson DR, Deerinck TJ, Marrs GS, Dehoff M, Wu J, Ellisman MH & Spirou GA (2013). Synaptic inputs compete during rapid formation of the calyx of held: A new model system for neural development. *J Neurosci* **33**, 12954–12969. https://doi.org/10.1523/JNEUROSCI.1087-13.2013

Hosogi N, Nishioka H & Nakakoshi M (2015). Evaluation of lanthanide salts as alternative stains to uranyl acetate. *Microscopy* **64**, 429–435. https://doi.org/10.1093/jmicro/dfv054

Hua Y, Laserstein P & Helmstaedter M (2015). Large-volume en-bloc staining for electron microscopy-based connectomics. *Nat Commun* **6**, 7923. https://doi.org/10.1038/ncomms8923

Ikeda KI, Inoue K, Kanematsu S, Horiuchi Y & Park P (2011). Enhanced effects of nonisotopic hafnium chloride in methanol as a substitute for uranyl acetate in TEM contrast of ultrastructure of fungal and plant cells. *Microsc Res Tech* **74**, 825–830. https://doi.org/10.1002/jemt.20964

Ishii N (2022). Systematic investigation of lanthanoid transition heavy metal acetates as electron staining reagents for protein molecules in biological transmission electron microscopy. *Microsc Microanal* **28**, 780–789. https://doi.org/10.1017/S1431927622000411

Ishii N & Odahara T (2023). Investigation of the efficacy of lanthanoid heavy metal acetates as electron staining reagents for biomembrane vesicles. *Microsc Microanal* **29**, 2080–2089. https://doi.org/10.1093/micmic/ozad107

Kaku H, Inoue K, Muranaka Y, Park P & Ikeda K (2015). Rapid contrast evaluation method based on affinity beads and backscattered electron imaging for the screening of electron stains. *Microscopy* **64**, 361–368. https://doi.org/10.1093/jmicro/dfv041

Kievits AJ, Duinkerken BHP, Fermie J, Lane R, Giepmans BNG & Hoogenboom JP (2024a). Optical STEM detection for scanning electron microscopy. *Ultramicroscopy* **256**. https://doi.org/10.1016/j.ultramic.2023.113877

Kievits AJ, Duinkerken BHP, Lane R, de Heus C, van Beijeren Bergen en Henegouwen D, Höppener T, Wolters AHG, Liv N, Giepmans BNG & Hoogenboom JP (2024b). FAST-EM array tomography: A workflow for multibeam volume electron microscopy. *Methods Microsc* **1**, 49–64. https://doi.org/10.1515/mim-2024-0005

Kievits AJ, Lane R, Carroll EC & Hoogenboom JP (2022). How innovations in methodology offer new prospects for volume electron microscopy. *J Microsc* **287**, 114–137. https://doi.org/10.1111/jmi.13134

Kubota Y, Sohn J & Kawaguchi Y (2018). Large volume electron microscopy and neural microcircuit analysis. *Front Neural Circuits* **12**, 98. https://doi.org/10.3389/fncir.2018.00098

Kuipers J & Giepmans BNG (2020). Neodymium as an alternative contrast for uranium in electron microscopy. *Histochem Cell Biol* **153**, 271–277. https://doi.org/10.1007/s00418-020-01846-0

Kuipers J, Kalicharan RD, Wolters AHG, van Ham TJ & Giepmans BNG (2016). Large-scale scanning transmission electron microscopy (nanotomy) of healthy and injured zebrafish brain. *J Vis Exp* (111), 53635. https://doi.org/10.3791/53635

Loomba S, Straehle J, Gangadharan V, Heike N, Khalifa A, Motta A, Ju N, Sievers M, Gempt J, Meyer HS & Helmstaedter M (2022). Connectomic comparison of mouse and human cortex. *Science* **377**, 6602. https://doi.org/10.1126/science.abo0924

Miyaki T, Homma N, Kawasaki Y, Kishi M, Yamaguchi J, Kakuta S, Shindo T, Sugiura M, Oliva Trejo JA, Kaneda H, Omotehara T, Takechi M, Negishi-Koga T, Ishijima M, Aoto K, Iseki S, Kitamura K, Muto S, Amagasa M, Hotchi S, Ogura K, Shibata S, Sakai T, Suzuki Y & Ichimura K (2024). Ultrastructural analysis of whole glomeruli using array tomography. *J Cell Sci* **137**, 20. https://doi.org/10.1242/jcs.262154

Moscardini A, Di Pietro S, Signore G, Parlanti P, Santi M, Gemmi M & Cappello V (2020). Uranium-free X solution: A new generation contrast agent for biological samples ultrastructure. *Sci Rep* **10**, 11540. https://doi.org/10.1038/s41598-020-68405-4

Nakakoshi M, Nishioka H & Katayama E (2011). New versatile staining reagents for biological transmission electron microscopy that substitute for uranyl acetate. *J Electron Microsc (Tokyo)* **60**, 401–407. https://doi.org/10.1093/jmicro/dfr084

Niedrig H (1978). Physical background of electron backscattering. *Scanning* **1**, 17–34. https://doi.org/10.1002/sca.4950010103

Odriozola A, Llodrá J, Radecke J, Ruegsegger C, Tschanz S, Saxena S, Rohr S & Zuber BB (2017). High contrast staining for serial block face scanning electron microscopy without uranyl acetate. *bioRxiv* https://doi.org/10.1101/207472

Pereira AF, Hageman DJ, Garbowski T, Riedesel C, Knothe U, Zeidler D & Knothe Tate ML (2016). Creating high-resolution multiscale maps of human tissue using multi-beam SEM. *PLoS Comput Biol* **12**, e1005217. https://doi.org/10.1371/journal.pcbi.1005217

Phelps JS, Hildebrand DGC, Graham BJ, Kuan AT, Thomas LA, Nguyen TM, Buhmann J, Azevedo AW, Sustar A, Agrawal S, Liu M, Shanny BL, Funke J, Tuthill JC & Lee W-CA (2021). Reconstruction of motor control circuits in adult Drosophila using automated transmission electron microscopy. *Cell* **184**, 759–774.e18. https://doi.org/10.1016/j.cell.2020.12.013

Rocklin M (2015). Dask: Parallel computation with blocked algorithms and task scheduling. *In SciPy*, 126–132. https://dask-local.readthedocs.io/en/latest/cite.html

Sawaguchi A, Kamimura T, Kitagawa K, Nagashima Y & Takahashi N (2024). KMnO4/Pb staining allows uranium free imaging of tissue architectures in low vacuum scanning electron microscopy. *NPJ Imaging* **2**, 40. https://doi.org/10.1038/s44303-024-00045-z

Seligman AM, Wasserkrug HL & Hanker JS (1966). A new staining method (OTO) for enhancing contrast of lipid–containing membranes and droplets in osmium tetroxide–fixed tissue with osmiophilic thiocarbohydrazide(TCH). *J Cell Biol* **30**, 424–432. https://doi.org/10.1083/jcb.30.2.424

Shapson-Coe A, Januszewski M, Berger DR, Pope A, Wu Y, Blakely T, Schalek RL, Li PH, Wang S, Maitin-Shepard J, Karlupia N, Dorkenwald S, Sjostedt E, Leavitt L, Lee D, Troidl J, Collman F, Bailey L, Fitzmaurice A, Kar R, Field B, Wu H, Wagner-Carena J, Aley D, Lau J, Lin Z, Wei D, Pfister H, Peleg A, Jain V & Lichtman JW (2024). A petavoxel fragment of human cerebral cortex reconstructed at nanoscale resolution. *Science* **384**, eadk4858. https://doi.org/10.1126/science.adk4858

Shibata S, Iseda T, Mitsuhashi T, Oka A, Shindo T, Moritoki N, Nagai T, Otsubo S, Inoue T, Sasaki E, Akazawa C, Takahashi T, Schalek R, Lichtman JW & Okano H (2019). Large-area fluorescence and electron microscopic correlative imaging with multibeam scanning electron microscopy. *Front Neural Circuits* **13**, 29. https://doi.org/10.3389/fncir.2019.00029

Ströh S, Hammerschmith EW, Tank DW, Seung HS & Wanner AA (2022). In situ X-ray-assisted electron microscopy staining for large biological samples. *eLife* **11**, e72147. https://doi.org/10.7554/eLife.72147

Sutton JS (1968). Potassium permanganate staining of ultrathin sections for electron microscopy. *J Ultrastruct Res* **21**, 424–429. https://doi.org/10.1016/S0022-5320(67)80150-3

van der Walt S, Schönberger JL, Nunez-Iglesias J, Boulogne F, Warner JD, Yager N, Gouillart E & Yu T (2014). scikit-image: Image processing in Python. *PeerJ* **2**, e453. https://doi.org/10.7717/peerj.453

Walton J (1979). Lead aspartate, an en bloc contrast stain particularly useful for ultrastructural enzymology. *J Histochem Cytochem* **27**, 1337–1342. https://doi.org/10.1177/27.10.512319

West M, Zurek N, Hoenger A & Voeltz GK (2011). A 3D analysis of yeast ER structure reveals how ER domains are organized by membrane curvature. *J Cell Biol* **193**, 333–346. https://doi.org/10.1083/jcb.201011039

Willingham MC & Rutherford AV (1984). The use of osmium-thiocarbohydrazide-osmium (OTO) and ferrocyanide-reduced osmium methods to enhance membrane contrast and preservation in cultured cells. *J Histochem Cytochem* **32**, 455–460. https://doi.org/10.1177/32.4.6323574

Yin W, Brittain D, Borseth J, Scott ME, Williams D, Perkins J, Own CS, Murfitt M, Torres RM, Kapner D, Mahalingam G, Bleckert A, Castelli D, Reid D, Lee W-CA, Graham BJ, Takeno M, Bumbarger DJ, Farrell C, Reid RC & da Costa NM (2020). A petascale automated imaging pipeline for mapping neuronal circuits with high-throughput transmission electron microscopy. *Nat Commun* **11**, 4949. https://doi.org/10.1038/s41467-020-18659-3

Zheng Z, Lauritzen JS, Perlman E, Robinson CG, Nichols M, Milkie D, Torrens O, Price J, Fisher CB, Sharifi N, Calle-Schuler SA, Kmecova L, Ali IJ, Karsh B, Trautman ET, Bogovic JA, Hanslovsky P, Jefferis GSXE, Kazhdan M, Khairy K, Saalfeld S, Fetter RD & Bock DD (2018). A complete electron microscopy volume of the brain of adult *Drosophila melanogaster*. *Cell* **174**, 730–743.e22. https://doi.org/10.1016/j.cell.2018.06.019

Zheng Z, Own CS, Wanner AA, Koene RA, Hammerschmith EW, Silversmith WM, Kemnitz N, Lu R, Tank DW & Seung HS (2024). Fast imaging of millimeter-scale areas with beam deflection transmission electron microscopy. *Nat Commun* **15**, 6860. https://doi.org/10.1038/s41467-024-50846-4

Zuidema W & Kruit P (2020). Transmission imaging on a scintillator in a scanning electron microscope. *Ultramicroscopy* **218**, 113055. https://doi.org/10.1016/j.ultramic.2020.113055